Computers & Geosciences 207 (2026) 106069

Contents lists available at ScienceDirect

Computers and Geosciences

journal homepage: www.elsevier.com/locate/cageo

Research paper

RIPPL, a Python-based InSAR stack and tropospheric delay software package

G. Mulder *, F.J. van Leijen, P. Lopez-Dekker, R.F. Hanssen

Delft University of Technology, Stevinweg 1, Delft, The Netherlands

ARTICLE INFO

Keywords:
InSAR
NWP model
Tropospheric delay
Sentinel-1
Python
Interferometry

ABSTRACT

Interferometric Synthetic Aperture Radar (InSAR) has a wide range of applications, including the monitoring of solid-earth and cryospheric geophysical processes and the monitoring of the built environment. The use of InSAR for atmospheric applications is less thoroughly developed. To perform such analyses the atmospheric phase delay of the SAR signal between different overpasses is used, which needs to be disentangled from other phase constituents, such as displacements and topography, which requires stack processing of large data volumes. Typically, initial atmospheric delays are predicted using existing numerical weather prediction (NWP) models, but InSAR processing and NWP model delay estimation software are not well integrated. Here we present a pure Python-based software package that integrates the automatic downloading and processing of InSAR and NWP model data to create time-series of unwrapped InSAR interferograms and InSAR equivalent tropospheric delays from NWP models. By combining the geometry of the InSAR radar signals with different NWP model datasets the tropospheric delays can accurately be derived on a pixel by pixel basis.

1. Introduction

SAR interferometry (InSAR) is a well established technique that utilizes the phase changes of radar waves between consecutive satellite overpasses to measure differences in signal delays in the order of millimetres (Hanssen, 2001). Topography, line-of-sight surface displacements between the different overpasses, and atmospheric signal delays due to the weather conditions during these overpasses are the main contributors to this signal, leading to products such as digital elevation models (DEMs), deformation maps of the earth's surface, buildings and infrastructure, and atmospheric delay maps. The latter have a large but under exploited potential to be used in numerical weather prediction (NWP) models.

For InSAR processing there are different software packages available, commercially, like Gamma (Wegmüller and Werner, 1997) or open-source, like Doris (Kampes and Usai, 1999), ICSE (Rosen et al., 2015), GMTSAR (Sandwell et al., 2011) and SNAP (ESA, 2021b).

With the launch of new SAR satellites, also the number of different operational modes of SAR satellites is evolving, which needs constant adaptation of software capabilities. Especially, the TOPSAR mode (De Zan and Guarnieri, 2006) and large data volumes of the Sentinel-1 satellites changed the requirements for InSAR software. Moreover, the particular usage of InSAR for atmospheric studies required a more robust integration with numerical weather prediction models (NWP).

To address the need for integrated processing, we developed the Radar Interferometric Parallel Processing Lab (RIPPL), a system optimized for handling Sentinel-1 TOPSAR mode data. RIPPL combines InSAR processing with atmospheric delay estimation derived from NWP models. This integration produces combined stacks of InSAR and NWP delay values, which can be used either to correct InSAR measurements for atmospheric effects or to improve the accuracy of NWP models using InSAR data. While the computation of atmospheric delays from NWP models has been implemented in other tools, such as GACOS (Yu et al., 2018), PyAPS (Jolivet et al., 2011), TRAIN (Bekaert et al., 2015), TropoDeep (Haji-Aghajany et al., 2025) or AtmNet (Zhou et al., 2023), these systems operate independent from the InSAR processing software. Because in RIPPL these two parts are integrated, it is much easier for users to create combined InSAR and NWP model delay time-series. Additionally, the RIPPL package also supports the use of the high-resolution CERRA (Ridal et al., 2024) and HARMONIE-AROME (Bengtsson et al., 2017) NWP model data, which are part of other packages. Finally, the radar geometry from InSAR processing can be used to compute NWP delay estimates, enabling the use of slant total delays (STD) (de Haan et al., 2009) rather than zenith total delays (ZTD) (Jolivet et al., 2011; Yu et al., 2018).

To simplify the use of the software it integrates the automatic download and processing of Sentinel-1 Single Look Complex (SLC) data (ESA, 2024), precise orbits (ESA, 2021a), SRTM (Farr et al., 2007) and TanDEM-X (Rizzoli et al., 2017) DEM data and ERA5

* Corresponding author.
E-mail address: gert.mulder@gmail.com (G. Mulder).

https://doi.org/10.1016/j.cageo.2025.106069
Received 7 February 2025; Received in revised form 16 October 2025; Accepted 17 October 2025
Available online 22 October 2025

Table 1
Different SAR, DEM and NWP input datasets from external sources used in RIPPL. All datasets are available free of charge, but for most datasets the user should register and provide their credentials during the RIPPL setup. The KNMI Dataplatform can only be used to download the most recent HARMONIE-AROME data, additional historical data is available on request.

Data type	Source	Provider	Link	Login
Sentinel-1 SLCs & orbits	Copernicus data space	ESA	dataspace.copernicus.eu/	Yes
Sentinel-1 SLCs & orbits	Alaska satellite facility DAAC	ASF	asf.alaska.edu	Yes
SRTM DEM	USGS data pool	USGS	lpdaac.usgs.gov	Yes
TanDEM-X DEM	EOC geoservice	DLR	download.geoservice.dlr.de	Yes
EGM96 geoid	NGA office of geomatics	USGS	earth-info.nga.mil	No
ERA5 NWP model	Copernicus climate data store	ECMWF	cds.climate.copernicus.eu	Yes
CERRA NWP model	Copernicus climate data store	ECMWF	cds.climate.copernicus.eu	Yes
HARMONIE-AROME NWP model	KNMI Dataplatform (last 4 days)	KNMI	dataplatform.knmi.nl	Yes

(Hersbach et al., 2020) and CERRA (Ridal et al., 2024) NWP model data. This allows users to easily integrate DEM and NWP model data in their processing chain.

In the RIPPL software package we implemented parallel processing of large InSAR datasets, while preserving the flexibility for researchers to adapt the processing to their own needs. This is done by keeping the RIPPL software a pure Python package and using the available Python tools to optimize for processing speed and data storage efficiency.

In the next sections we first give an overview of the developed method for InSAR and NWP model processing steps in the RIPPL package. Secondly, we focus on how the processing and data handling is implemented in the software to allow efficient parallel computations. Thirdly, we give two case studies for the InSAR and NWP model processing that are available as a tutorial in the RIPPL package. Finally, we conclude with a discussion

2. Theory

In this section we explain the used processing principles for InSAR processing and the developed methods to calculate the expected InSAR tropospheric delays from NWP models.

2.1. Stack processing approach

The setup of the RIPPL software is built around the interferometric stack. This is a set of SAR SLC images for different satellite overpasses for the same satellite track, which are coregistered to the same reference image for interferometric processing. These SLC images are provided by different space agencies or companies and derived from raw SAR data using Doppler centroid estimation, range migration and azimuth focusing (Hanssen, 2001). Due to the Sentinel-1 TOPSAR Interferometric Wide (IW) swath mode, the images are first split in individual bursts or slices and coregistered to the referenced SLC. After the coregistration the slices are combined to a full image and converted to geographic or projected coordinate systems using resampling of multilooking. The results of the different processing steps of individual SLCs or interferograms are outputted in the same folder and summarized in a json meta data file, see Figs. 1 and 5.

2.2. Main processing steps Sentinel-1 processing

For the interferometric processing of InSAR data, RIPPL applies a number of processing steps that are well described in InSAR literature, see e.g. Hanssen (2001), Moreira et al. (2013) and Yague-Martinez et al. (2016), see Fig. 1. This is the default setup for InSAR processing in RIPPL, but can be adjusted by adding or changing individual processing steps.

To create a RIPPL stack the user needs to define the area of interest, period of interest and the specific satellite track, see Fig. 1 top left. Based on these user inputs the SLC data, needed DEM data and the precise satellite orbits are downloaded from external sources, which are listed in Table 1. Then all SLCs are geo-referenced, coregistered and resampled to the grid of the reference SLC to allow the creation of interferograms. Because most processing steps are specific for the reference SLC, other SLCs or interferograms only, all steps Fig. 1 are divided of these three image types.

After the download of all relevant SAR, DEM and orbit data, the user selects one reference SLC, which radar coordinates are used as reference for all other SLCs. This reference SLC image is then geo-referenced using a newly created DEM in radar coordinates. In this step every radar coordinate in range and azimuth $(\mathrm{ra}, \mathrm{az})$ is linked with a geographic coordinate in latitude, longitude and ellipsoidal height $(\mathrm{lat}, \mathrm{lon}, h)$. Because the SLC is already processed from raw SAR data using the zero-Doppler geometry, this can be done by intersecting the iso-range circle with the topographic surface of the Earth in the zero-Doppler plane, perpendicular to the satellite orbit, see Fig. 2 (Geudtner and Schwäbisch, 1996). To find the DEM with the topographic height of every radar pixel as input for geocoding, the needed heights for the radar coordinates are interpolated from external DEM data for the area of interest, which can either be SRTM (Farr et al., 2007) or TanDEM-X (Rizzoli et al., 2017) at 30 or 90 m resolution. This is done by converting the $(\mathrm{lat}, \mathrm{lon})$ coordinates of the original DEM to radar coordinates (Kampes and Hanssen, 2004), which is then triangulated (Virtanen et al., 2020) and interpolated to the regular radar grid using barycentric interpolation.

Using the estimated geographic coordinates of the reference SLC, all other SLCs are coregistered to the reference radar grid using a geometric coregistration (Sansosti et al., 2006), which results in a range and azimuth shift for every individual pixel. These pixel shifts are then used to resample other SLCs based on resampling kernels given by Hanssen (2001). However, in the case of TOPSAR acquisition the SLC is not a baseband signal, due to the azimuth-varying non-zero Doppler centroid, which is required for resampling based on these kernels. Therefore, prior to the interpolation the signal is *deramped* (Yague-Martinez et al., 2016). After any additional range or azimuth filtering is applied, resampled TOPSAR SLCs can be reramped again to allow interferogram creation.

A large part of the phase differences in interferograms are due to surface topography, which can be closely approximated using external DEMs. Therefore, the topographic phase shifts are first removed in the phase correction step for all but the reference SLC. A set of interferograms can then be created using different combinations of coregistered SLCs. Currently supported option are: (1) all possible interferometric combinations, (2) all interferometric combinations with the reference image only and, (3) all interferometric combinations with a maximum temporal baseline. These can be used respectively for the SqueeSAR algorithm (Ferretti et al., 2011), single-reference PS processing (Ferretti et al., 2001) and small baseline subsets (SBAS) approach (Berardino et al., 2002). For every interferogram also the coherence is estimated (Touzi et al., 1999), which is often needed for the above mentioned method. Finally, the RIPPL package uses SNAPHU (Chen and Zebker, 2002) to perform an unwrapping of the data.

To use the InSAR output data in common GIS software and reduce the image size, the interferogram, coherence, amplitude and unwrapped output images can be converted to a geographic or projected grid. Example results for the interferogram, calibrated amplitude, coherence and unwrapped interferogram are given in Fig. 10.

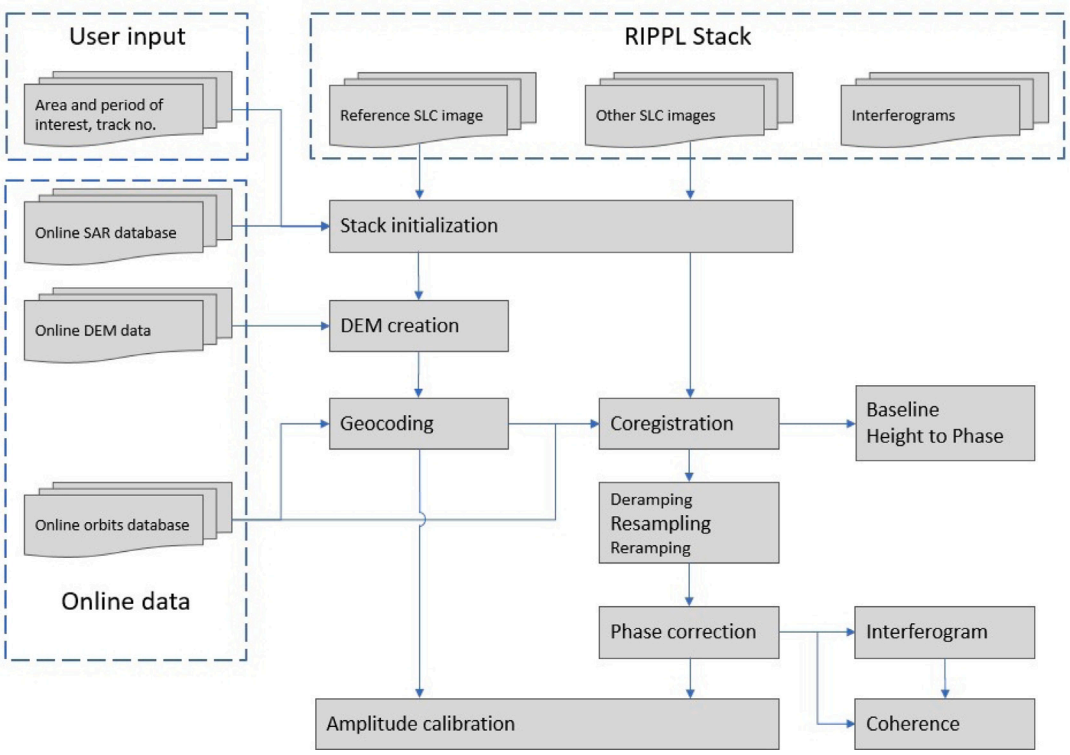

Fig. 1. Main steps for InSAR processing. On the left the user inputs and the online data are given, which are downloaded as part of the RIPPL processing. On top the structure of the RIPPL stack is given, which consists of (i) one reference SLC, (ii) one or multiple other SLC images which are coregistered and resampled to the reference SLC and (iii) one or multiple interferograms of the SLC images in the stack. For these three image types the relevant processing steps are given column-wise. Regular stack processing starts with stack initialization followed by DEM generation and geocoding of the reference SLC. Then the other SLCs are coregistered, resampled and phase corrected. The coregistered stack of SLCs is then used to create interferograms, and coherence and radiometric calibrated amplitude images. As a last step the interferograms can be unwrapped, using SNAPHU (Chen and Zebker, 2002).

2.3. Tropospheric delay estimation

The second main component of the RIPPL package is the calculation of tropospheric delays from NWP models. Currently it is possible to process NWP model data from the ERA5 (Hersbach et al., 2020) and CERRA (Ridal et al., 2024) reanalysis models provided by the European Centre for Medium-Range Weather Forecasts (ECMWF) and the HARMONIE-AROME model (Bengtsson et al., 2017) provided by the Royal Netherlands Meteorological Institute (KNMI). The coverage of the NWP models are Western-Europe for the HARMONIE-AROME model, worldwide for the ERA5 model and Europe-wide for the CERRA model. The needed data for the ERA5 and CERRA models can be downloaded automatically from the Copernicus climate data store (ECMWF, 2019). The HARMONIE-AROME data should be acquired at the KNMI or one of the 11 other European national weather services using the HARMONIE-AROME model.

To convert the obtained weather model data to InSAR atmospheric delays, NWP model parameters are converted to refractivity and integrated along the slant path of the radar signal from the ground to the satellite sensor, see Fig. 2. The total derived atmospheric delay δ is given by,

$$\delta = \int_{\text{scat}}^{\text{sat}} N(z)dz, \tag{1}$$

where $N(z)$ is the refractivity of air at location z between the scatterer on the ground scat and the satellite sat. Refractivity values are mainly dependent on dry air pressure P_d, water vapour pressure e and temperature T, and can be modelled as (Davis et al., 1985)

$$N = k_1\frac{P}{T} + k_2'\frac{e}{T} + k_3\frac{e}{T^2} + k_4\frac{n_e}{f^2} + k_5 W, \tag{2}$$

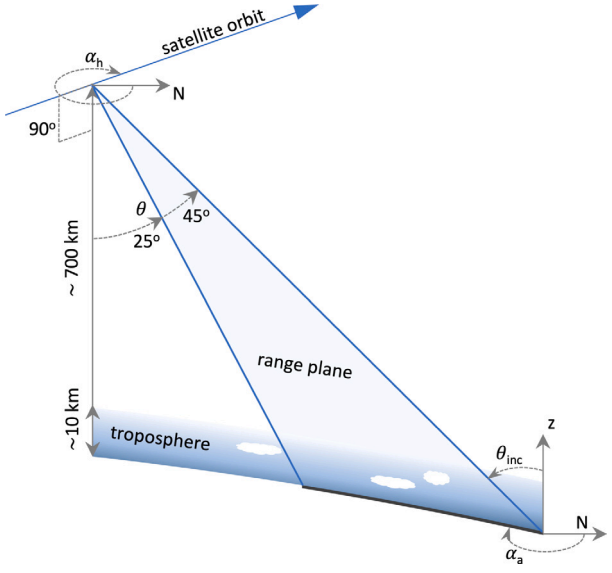

Fig. 2. The satellite geometry of the Sentinel-1 satellite mission. The radar signal travels within the range plane, which is on average perpendicular to the satellite heading α_h. The radar satellite observes a swath with a width of about 250 km with a range in look-angles θ of approximately 25 to 45 degrees. The tropospheric delays depend on the pressure, temperature and specific humidity along the slant satellite path, which is defined by the location on the ground (lat,lon, h), incidence angle θ_{inc} and azimuth angle α_a.

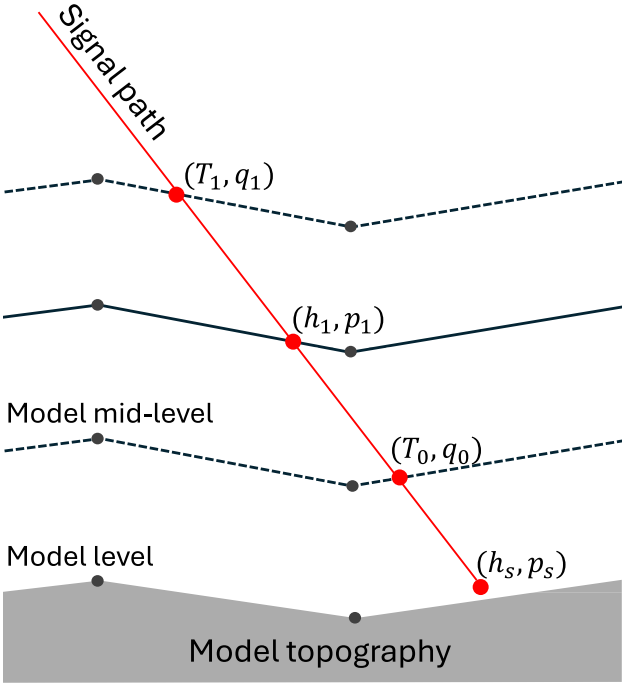

Fig. 3. Illustration of slant ray-tracing technique. This shows how the atmospheric delay values are derived along a straight path between the scatterer and the satellite, ignoring the minimal bending of the signal path. Based on the pressure difference ΔP, temperature T and specific humidity q the delay per model layer is calculated and integrated of the full signal path. For the lowest model layer the height and pressure values of the scatterer are used instead of the bottom of the model layer.

where T is temperature in Kelvin, e is the partial pressure of water vapour, P_d the partial pressure of dry air, L the liquid water content, n_e is the electron density per cubic metre, f the radar frequency and W the liquid water content. The values of the constants are $k_1 = 77.6\,\mathrm{K\,h\,Pa^{-1}}$, $k_2' = 23.3\,\mathrm{K\,h\,Pa^{-1}}$ and $k_3 = 3.75 \cdot 10^5\,\mathrm{K^2\,h\,Pa^{-1}}$, and $k_4 = -4.028 \times 10^7\ \mathrm{m^{-3}}$, $k_5 = 1.4\ \mathrm{m^3\ g^{-1}}$. The last two terms represent the ionospheric refractivity and the refractivity due to liquid water in the atmosphere. However, the ionospheric is spatially smooth and therefore mainly creates an offset for the whole image (Meyer, 2011). Additionally, the contribution of liquid water is minimal and can be left out in further calculations (Hanssen, 2001).

To derive the total slant delay we use a direct line and plane intersection approach, assuming that the radar signal travels in a straight line from the scatterer to the satellite within the zero-Doppler plane. This allows us to calculate the actual slant delay instead of deriving it from the vertically integrated zenith delay using a simple mapping function, like in GACOS (Yu et al., 2018), PyAPS (Jolivet et al., 2014), TRAIN (Bekaert et al.) and TropoDeep (Haji-Aghajany et al., 2025). In reality the slant delay signal is also bended (Thayer, 1967), which is often used for the assimilation Global Navigation Satellite System (GNSS) measurements (De Haan, 2008). However, this effect is minimal for InSAR because the incidence angle is below 45°, leading to a max deviation of 0.04° at ground level (Huuskonen and Holleman, 2007). This leads to absolute delay differences of less then 1 mm delay and even smaller relative differences, which are not significant. Therefore, the main focus in this approach is on how to convert pressure and model level data to a grid of pressure and height coordinates in the zero-Doppler plane, to allow piecewise integration along the slant path of the radar signal, see Fig. 2. First the NWP model values are interpolated onto the zero-Doppler plane to allow ray-tracing in this 2D plane. Then the pressure and height coordinates (h, p) of the model levels are calculated, assuming hydrostatic balance (De Haan, 2008). Then the path of the signal is tracked and used to interpolate (T, q) values at mid-level, see Fig. 3. Based on these parameters the piecewise integrated delay $\delta^t_{\mathrm{NWP},l}$ is calculated (De Haan, 2008),

$$\delta^t_{\mathrm{NWP},l} = \frac{1}{\sin\theta}\left(k_1\frac{R_d}{g_h}\Delta P + k_2'\frac{R_v}{g_h}q\Delta P + k_3\frac{R_v}{g_h T}q\Delta P\right), \tag{3}$$

where ΔP is the pressure difference between the top and bottom of the model layer l at time t, R_d and R_v are the gas constants for dry and moist air, g_h the gravity at given height h, q is the specific humidity of the model layer, T is the temperature of the model layer and θ is the incidence angle of the satellite signal. The total delay is then,

$$\delta^t_{\mathrm{NWP}} = \sum_{l=1}^{n} \delta^t_{\mathrm{NWP},l}, \tag{4}$$

where δ^t_{NWP} is delay for n model levels. The RIPPL package also includes options to separate the hydrostatic and wet delay (Bevis et al., 1992) to distinguish delay differences due to air pressure and water vapour variations. This is done by splitting Eq. (3) into a hydrostatic and wet part and integrating them like Eq. (4). Similarly, the package includes an option to derive the non-topographic tropospheric delay, which is done by setting the input heights of all scatterers to zero. The software implementation of this ray-tracing method is further discussed in Section 3.5. Results from the tutorial to calculate the InSAR, HARMONIE-AROME, CERRA and ERA5 tropospheric delays are given in Fig. 11.

3. Software implementation

After description of the used algorithms for InSAR processing in the former section, this section describes how these algorithms are implemented to create a pure Python package that is extendable and includes parallel processing. First we discuss the data structure to store InSAR (meta)data on disk. Then we explain how RIPPL works with different types of coordinate systems and how multilooking and resampling methods are used to convert between coordinate systems. Finally, we focus on how the parallel, in-memory processing is implemented.

3.1. Data structure

To store the InSAR stack on disk a folder structure is created with separate folders for individual SLCs and interferograms. Every SLC or interferogram folder contains processing outputs as binary (.raw) files and one meta data file stored as a javascript object notation (.json) file, see Fig. 5. This meta data file contains all the relevant information about the satellite sensor, acquisition mode, satellite orbits and applied processing steps. For every processing step this list all the input parameters and details about the input and output data, including data paths, data types, data sizes and coordinate systems. Using the meta data all processing outputs can be read as numpy memory-maps (Harris et al., 2020), which makes the files easy accessible for further processing steps but does not load them in memory.

3.2. Radar coordinates and satellite geometry

An important part of the interferometric processing is the geocoding and coregistration of SAR data in radar coordinates, which are directly linked to the observation geometry of the SAR sensor. To derive the observation geometry for the Sentinel-1 data both the SLC data and orbits are needed, which are both downloaded from the Copernicus Data Space Ecosystem (ESA, 2021a). After downloading the orbits are interpolated using cubic splines to find the Cartesian coordinates (x, y, z), direction vectors (x', y', z') and acceleration vectors (x'', y'', z'') for every radar image line in azimuth direction. This orbit information is then used to estimate the geographic coordinates $(\mathrm{lat}, \mathrm{lon}, h)$ of the radar pixels during geocoding, see Fig. 6. Based on the satellite orbit and geographic coordinates of the radar pixels further geometric parameters such as the look angle, heading, incidence angle, azimuth angle can be calculated, see Fig. 2.

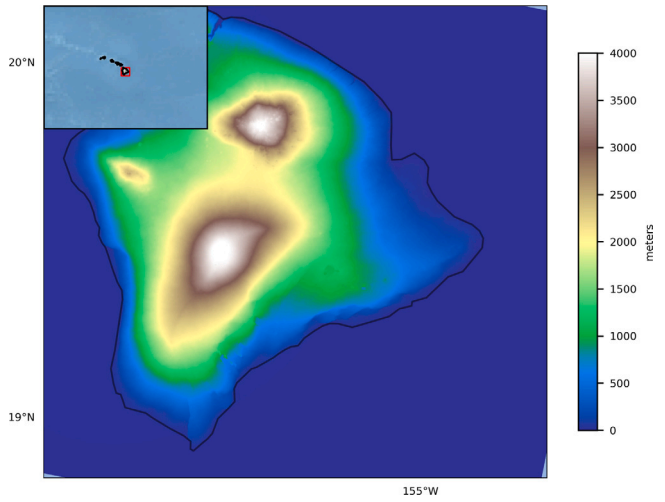

(a) SRTM DEM of the Hawaii island.

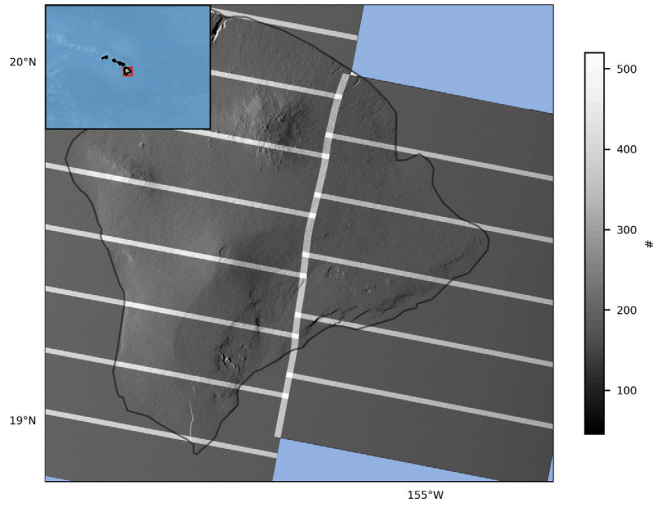

(b) Number of pixels per grid cell in an equidistant projected grid.

Fig. 4. Comparison between the DEM and the number of pixels per grid cell of an equidistant projected grid. This clearly shows the overlapping regions of the Sentinel-1 bursts, which results in up to three times higher number of pixels in the overlapping regions. It also shows the effect of a sloping terrain in line-of-sight direction on the horizontal range distance, see also Fig. 6. Other patterns shown in the number of pixels image is due to the fact that the geographic grid size does not fit exactly with a rounded number of range/azimuth cells, causing an alternating pattern.

3.3. Resampling, multilooking and merging of slices

Based on the found geographic coordinates $(\text{lat}, \text{lon}, h)$ during geocoding, the radar grids can now be resampled to other coordinate systems. First the other SLCs are resampled to the reference SLC grid using a sinc-based kernel resampling (Hanssen, 2001). Then the resampled grids are resampled to a geographic or projected grid defined by a proj4 string (PROJ contributors, 2021). To apply the different resampling steps a combination of sinc-based kernel resampling, multilooking and barycentric resampling are used, see Fig. 7. Kernel resampling is used for SLC data when the grid spacing of the new grid is similar to the old grid. Multilooking is used when the grid spacing of the new grid is larger than the original grid. Barycentric resampling is used when the input grid is irregularly spaced.

However, the different coordinate systems of the in- and output grid for resampling makes parallel processing more difficult. In case the in-

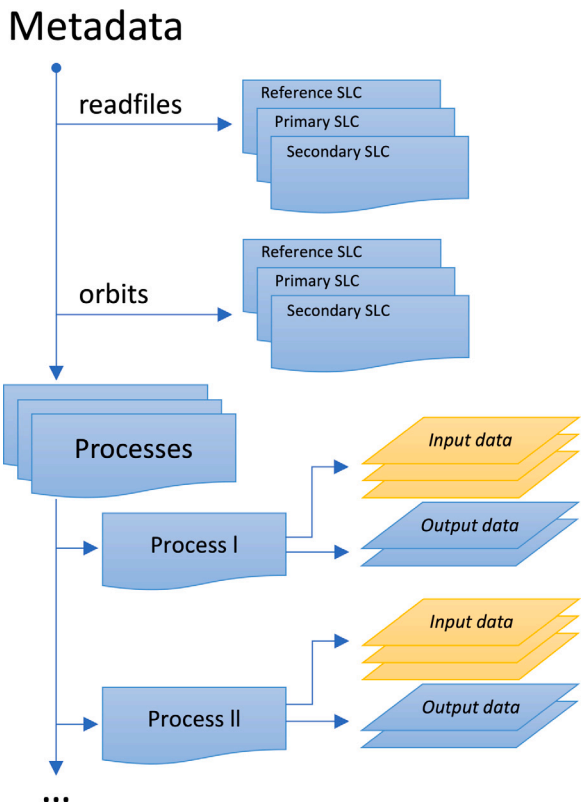

Fig. 5. Setup of the .json meta data file used for all images and slices in the InSAR stack. First the relevant meta data about the SAR sensor and source files are given in the readfiles section, followed by the satellite orbits in the orbits section. Then for all applied processing steps for the image the specific settings and input/output data are given.

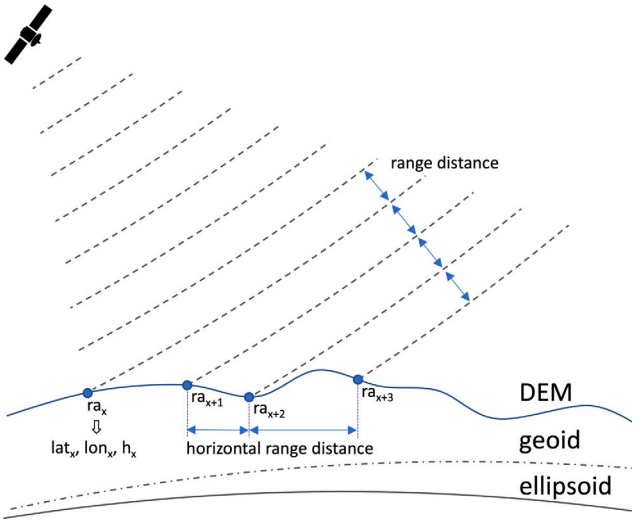

Fig. 6. Visualization of the geocoding process where geographic coordinates of the satellite range bins are calculated using the satellite position, orientation of the zero-Doppler plane and topography. To describe the topography a DEM with respect to the ellipsoid is, hence DEMs with respect to a geoid should be converted first. This also shows that although the range distances from the satellite line-of-sight are equally spaced, this does not translate to an equal range distance in horizontal direction, due to variation in topography and incidence angle θ_{inc}.

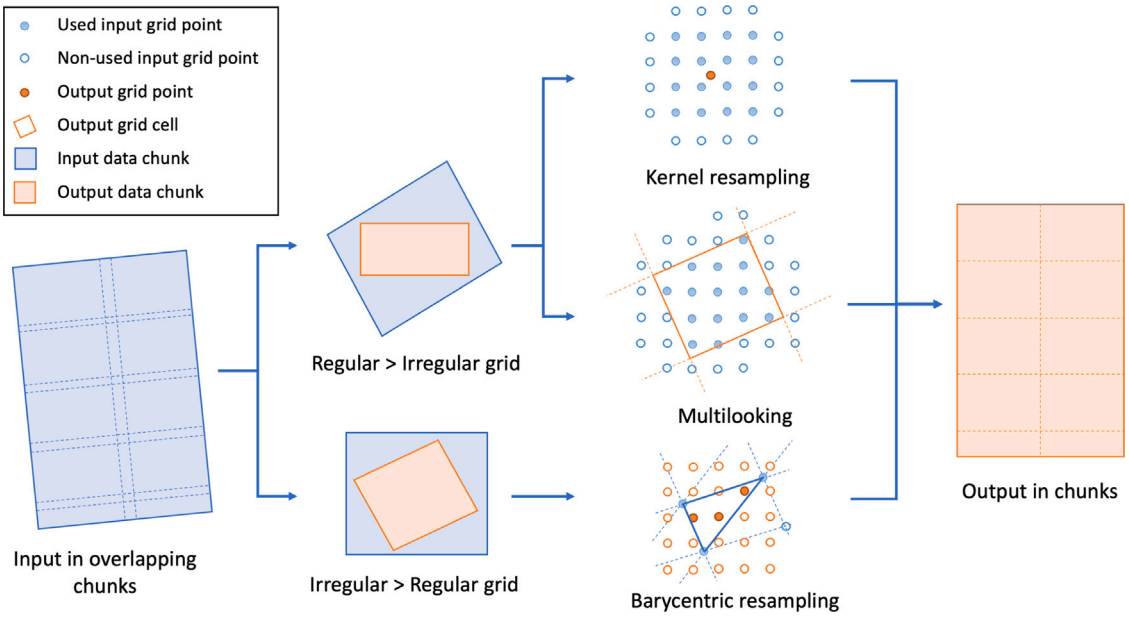

Fig. 7. Visualization of three types of resampling processes implemented in RIPPL. (1) Using kernel resampling the value of every output grid point is calculated based on a kernel of x by x input grid points (in this image $x = 4$). (2) Using multilooking all input grid points within the boundaries of a grid cell in a newly defined coordinate system are averaged. (3) Using barycentric resampling a triangulation is done for the irregular input grid and a barycentric interpolation is done for all output grid points within every triangle. Resampling is done in the input coordinate system for kernel resampling and multilooking and in the output coordinate system for barycentric resampling. To allow parallel processing, the newly defined output grid is split in chunks and for every chunk the minimum needed chunk size of the input grid is calculated, based on the conversion between different coordinate systems. This will lead to overlapping chunks in the input dataset.

and output grid have the same coordinates, they can easily be divided in different chunks and processed separately, using python packages like Dask (Dask Development Team, 2016), which is not the case when a grid is resampled. Therefore, the needed size of the input chunks is first calculated based on the input coordinates of the boundaries of the output chunk. This will create overlapping input chunks but independent output chunks, which prevents writing of different parallel processes to the same place in the output file, see Fig. 7.

3.4. Pipelines and parallel processing

To process large datasets of InSAR data the RIPPL software implements both parallel processing using multiple processors and pipelines which combine different processing steps without reading or writing to disk. This saves processing time, but also saves on disk IO and reduces the amount of disk space needed. Fig. 8 gives an example of a pipeline for the resampling and topographic phase correction. The figure shows on the left of the image the initial data inputs, in the middle the different in-memory processing steps and on the right the final resampled output data. Because the coordinates of the DEM and secondary SLC are different from the reference SLC, the data chunks loaded from these datasets will be overlapping as shown in Fig. 7.

Although most processing steps could be done in one pipeline, this is often not recommended due too code limitations or efficiency considerations. (1) Because any data chunks with a coordinate system other than the final output are overlapping, these data files cannot be saved to disk. (2) When the pipeline includes subsequent resampling steps the overlapping areas will become increasingly large for every resampling step, causing inefficient processing and memory use. (3) When processing a stack of images, some processing steps like geocoding will generate the same outputs for every secondary SLC or interferogram, which makes it more efficient to run and save these steps first.

Building and running a pipeline is done using the following steps.

1. **Initialization:** During the initialization of the pipeline we define the number of cores used for processing and the chunk size for every individual process.
2. **Processing steps:** The different processing steps for the pipeline are added in order. For example, the coregistration step should be added before the resampling step.
3. **Parallel run:** After setting the processing steps and input data the pipeline can be run. The data is automatically divided in different chunks and the pipeline is checked for any inconsistencies in the data or processing steps. If all checks are passed successfully the data is processed in parallel.

3.5. Tropospheric delay calculations

To calculate the NWP model delays the ray-tracing algorithm, as discussed in Section 2.3, is dependent on the already calculated radar geometry. Fig. 9 shows the subsequent calculation steps and how they depend on the satellite geometry. In the first step the weather model parameters are loaded and converted into refractivity values. In the second step the obtained refractivity values are interpolated for the zero-Doppler plane. In the third step the calculated refractivity values for the zero-Doppler planes are used to do the ray-tracing in a 2D plane using the incidence angle of the pixel.

Because the NWP model has a lower resolution than the InSAR data the surface elevation in the model does not coincide with the DEM used for InSAR processing. Therefore, the NWP model delay value is adjusted for height differences using linear interpolation.

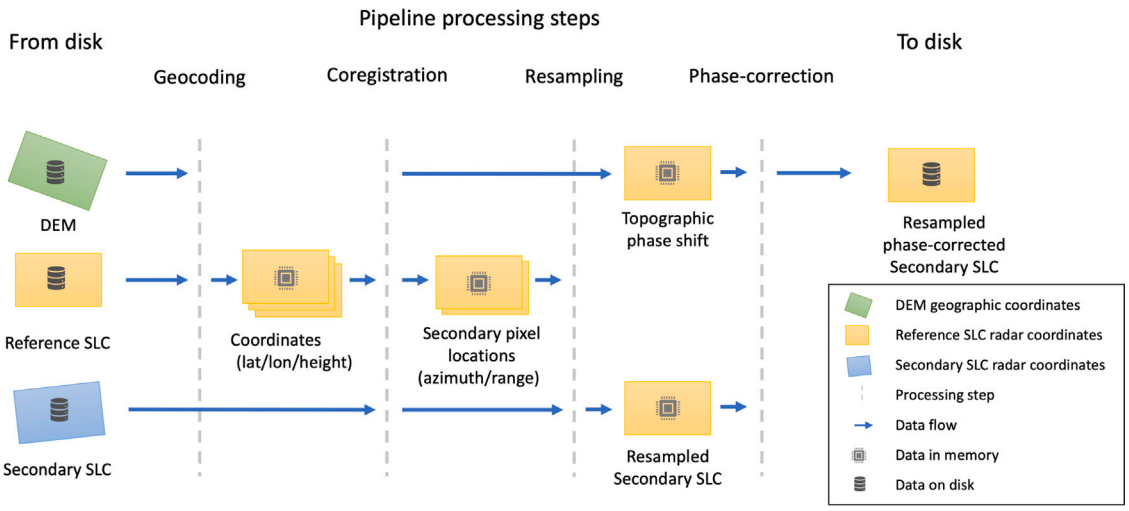

Fig. 8. Overview of a RIPPL processing pipeline. In this processing pipeline a secondary SLC is coregistered and resampled to the radar grid of the reference SLC. On the left the input datasets are given that are loaded from disk to memory before the processing starts. These are a DEM, the reference SLC and the secondary SLC in different coordinate systems. Then these datasets are processed using a geocoding, coregistration, resampling and phase-correction processing step, where all intermediate data is stored in memory. Finally, only the resampled phase-corrected secondary SLC is saved to disk. Using such a pipeline strongly reduces the needed disk space and the time needed to read and write data to and from disk. To allow parallel processing images are divided in chunks and processed separately, see Fig. 7. In this pipeline barycentric resampling is applied during the geocoding step and kernel resampling is done during the resampling step.

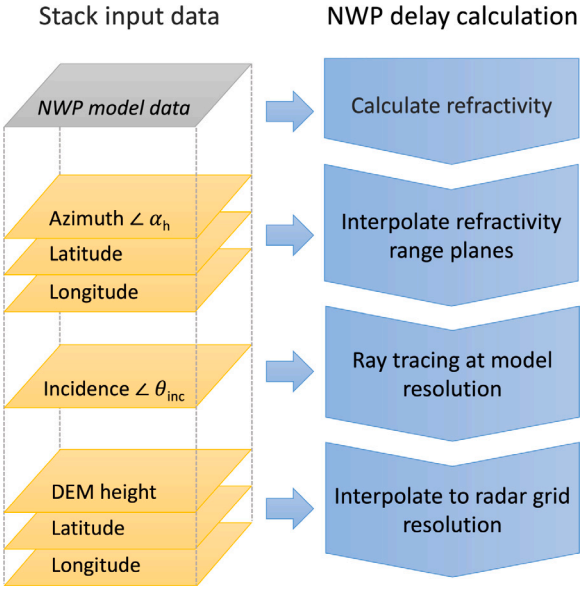

Fig. 9. Main steps in NWP delay calculations. On the right the different calculation steps to calculate tropospheric delays are given and on the left the corresponding input datasets from the InSAR stack that are needed to do this calculation. The NWP model data input is shown in a different colour here because it has the coordinate system and grid size of the original downloaded NWP model data, while all other datasets share the same coordinate system defined during the InSAR processing. Apart from the NWP model data, all input datasets are related to the satellite geometry, see Figs. 2 and 6.

3.6. Code adaptability

An important part of the RIPPL code is the ability to add or adapt processing steps. This can be done by adapting the processing step template, which is split in two parts: (i) The initialization function that defines the needed input data and created output data of the function (ii) The process calculations, which define the calculations done in this step using any Numpy (Harris et al., 2020) function. These steps can then be added to a pipeline as described in Section 3.4.

3.7. Processing outputs

In case the user would like to do post-processing in Python, the output data can directly be accessed as memmap files, which can be loaded from the stack object. Otherwise, data can be exported to .geotiff files. To visualize the results a plotting routine within the RIPPL software can be used, based on the cartopy package (Met Office, 2015). The .geotiff and plotting tools from the RIPPL software are limited to geographic or projected datasets. Examples of outputs are shown as part of the tutorials given in Section 4.

4. Results

To make the RIPPL software more accessible for first time users, we included two tutorials in the software package itself, which are written in the form of a Jupyter notebook. The advantage of this system is that the code can be run step by step, where the results can directly be visualized and the code is explained in detail. The first tutorial covers the main processing steps for an InSAR datastack, see Section 2.2, and highlights the effects of an earthquake on Hawaii in May 2018. The second tutorial focuses on the NWP model data, for a case over The Netherlands.

4.1. Earthquake Hawaii

The tutorial that comes with the RIPPL software includes a study case about the earthquake on the island of Hawaii on May 4th 2018.

Processing is done based on the main processing steps, see Section 2.2, and also includes unwrapping of the created multilooked interferogram. The main processing steps are combined in a minimum number successive pipelines to allow parallel processing and minimize disk usage. Because individual pipelines are limited to the use of two different coordinate systems, three different pipelines where needed for the conversion from DEM coordinates to radar coordinates, the resampling of the secondary SLC and the conversion from the reference radar grid to a multilooked grid in an oblique Mercator projection. The

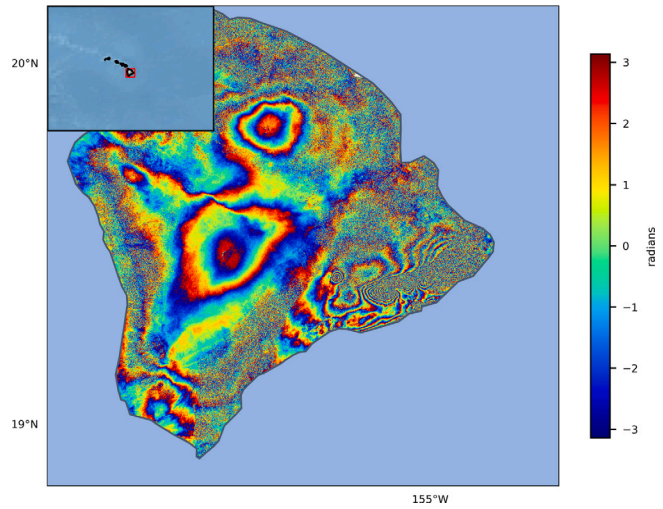

(a) Interferogram between 23rd of April and 5th of May 2018.

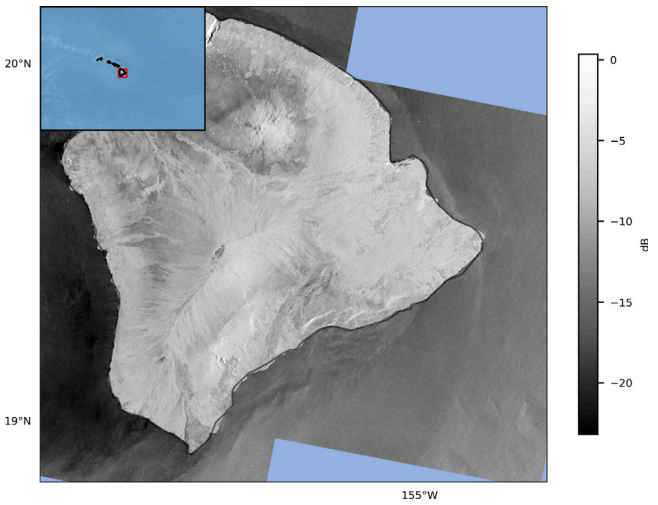

(b) Calibrated amplitude β^0 for the 23rd of April 2018.

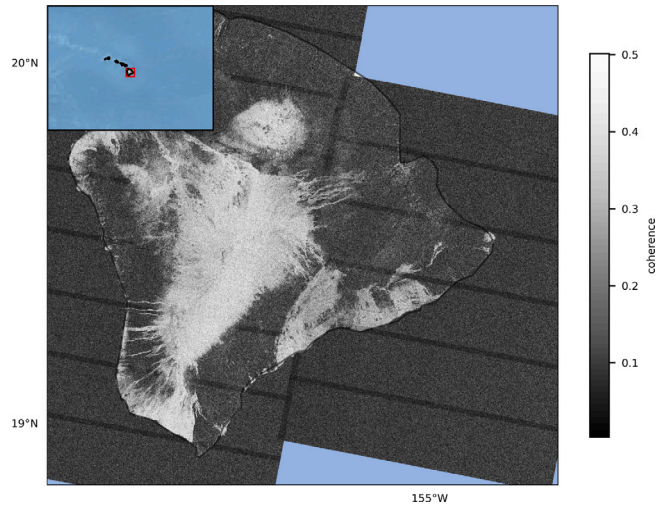

(c) Coherence between 23rd of April and 5th of May 2018.

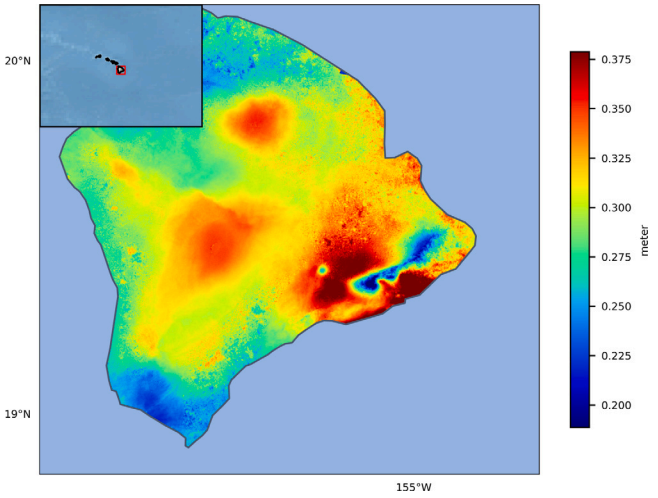

(d) Unwrapped interferogram.

Fig. 10. This figure gives an example of the direct output from RIPPL for an earthquake over Hawaii, which illustrates the capabilities of the software for InSAR processing. For the interferogram and unwrapped interferogram values over water are masked. The coherence image clearly shows lower values in the overlapping regions of the Sentinel-1 bursts, related to the higher number of pixels in these regions, see Fig. 4. This is due the smaller bias in the coherence estimates for low coherence values (Hanssen, 2001).

pipelines are preceded by the download of Sentinel-1 SLCs, Sentinel-1 precise orbits and SRTM DEM data, followed by the initialization of the stack.

The results for the interferogram, calibrated amplitude, coherence and unwrapped interferogram are given in Fig. 10. The images are created using the cartopy package (Met Office, 2015) and are also available as geotiffs, which is compatible with most geographic information system (GIS) software. Fig. 10a shows the highest density of fringes in the South-Eastern part of the island close to the epicentre of the earthquake. The unwrapped image shows a movement up to about 40 cm in the radar line of sight. Next to the fringes in the South-East part of the island, the interferogram also shows a few fringes in the centre of the island, which are not related to the earthquake but are due to the differences in the stratified atmosphere between the two epochs.

This example shows that the RIPPL software can be valuable tool for solid earth applications and does make full use of the available overlapping areas between the Sentinel-1 burst, see Fig. 10(c). However, it still has some difficulties with the unwrapping of areas with a high number of fringes or high noise levels. This could be solved by including filtering techniques (Goldstein and Werner, 1998) or combining the software with alternative unwrapping techniques (Hooper et al., 2007).

4.2. Weather model evaluation over the Netherlands

The second tutorial also runs the main steps to process the InSAR data, but includes the NWP model results for the HARMONIE-AROME model, provided by the KNMI, and the ERA5 en CERRA models, provided by the ECMWF. This shows that in this case a large part of the InSAR phase differences are due to the differences in tropospheric delays. The processing of NWP delays next to the InSAR delays can therefore be very helpful tool to either correct for tropospheric delays or to evaluate the use of InSAR phase differences for NWP models. The RIPPL code was therefore an important tool for the comparison and integration of InSAR and NWP model delays in Mulder et al. (2022). The InSAR and NWP model results are shown alongside in Fig. 11.

This figure shows that there is a clear correlation between the models resolution and the capability to capture details of the water vapour field. However, the details found with higher resolution do not always represent the real weather situation, as can be seen in Fig. 11d.

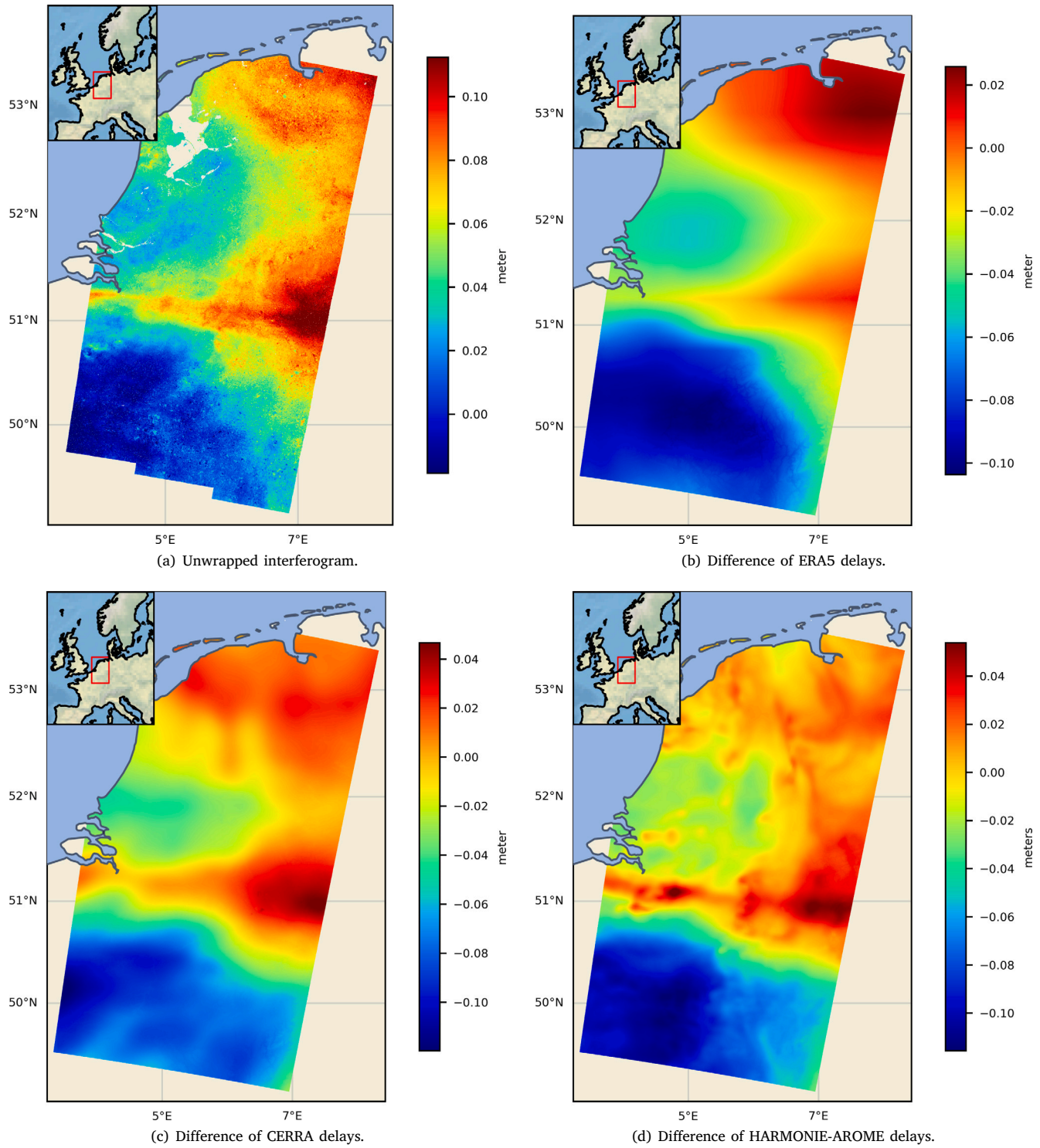

(a) Unwrapped interferogram.

(b) Difference of ERA5 delays.

(c) Difference of CERRA delays.

(d) Difference of HARMONIE-AROME delays.

Fig. 11. This figure shows a comparison between RIPPL InSAR results and derived NWP model delays. This data can be an input for tropospheric corrections of InSAR data, but can also be used to improve NWP model performance. Figure a gives the unwrapped interferogram between 18th and 24th of July 2017 over The Netherlands. Figures b,c and d show the modelled differential tropospheric delays from low to high-resolution for the ERA5 (30 km), CERRA (5.5 km) and HARMONIE-AROME (2.5 km) models. Note that the values for the interferogram are shifted compared to the model values. This is because InSAR can only measure relative delays and no absolute delays, which causes a shift in the absolute values.

This is mainly because high-resolution NWP models are able to capture small weather vapour patterns, but they are often in the wrong location. Further discussion on this can be found in Mulder et al. (2022, 2025).

4.3. Further case studies

In Sections 4.1 and 4.2 we showed two examples on how the RIPPL package can be used for short time-series, but the length and number of time-series can easily be expanded. Therefore, additional output data of two time-series with a time-span of one year are added in the additional materials of this paper. The presented cases are (1) An extension of the time-series over the Netherlands, including ERA5 and CERRA analysis and, (2) A time-series of InSAR images over the Patagonian Ice Fields, showing Sentinel-1 results over ice fields during different seasons.

5. Discussion

The combination of InSAR and NWP model delay values, as discussed in Section 4.2, has several applications, which is discussed in the following paragraphs.

5.1. InSAR tropospheric corrections

The most common use of InSAR tropospheric delay products is mitigating atmospheric effects in InSAR deformation studies. This approach is particularly useful for correcting large-scale phase trends or topographically induced delays. Well known packages are PyAPS (Jolivet et al., 2011), TRAIN (Bekaert et al., 2015) and GACOS (Yu et al., 2018), which all offer tropospheric delay products based on different NWP models. A comparison by Murray et al. (2019) showed that GACOS performed best, which is likely due to the high quality and spatial resolution (9 km) of the input data from the ECMWF HRES model. Additionally, external measurements can be combined with the derived NWP products using deep-learning methods to enhance the final product, for example, using DEMs like in AtmNet (Zhou et al., 2023) or GNSS measurements like in TropoDeep (Haji-Aghajany et al., 2025). Currently this mainly leads to improvement of delay products in areas with high GNSS cover, but with the integration other sources like rainfall radars this could lead to enhanced tropospheric delay products in the future.

In the RIPPL code automatic download and delay calculation of the worldwide ERA5 reanalysis (31 km resolution) and the Europe-wide CERRA reanalysis (5.5 km resolution) are implemented. For the HARMONIE-AROME (2.5 km resolution), only the delay calculation is included. This suggests RIPPL may perform better over Europe, especially in regions with lower GNSS coverage. However, higher resolutions do not always lead to significant improvements since precise timing and positioning of turbulent features becomes a limiting factor (Bekaert et al., 2015; Murray et al., 2019; Haji-Aghajany et al., 2025; Mulder et al., 2025).

In contrast with other packages RIPPL combines both InSAR processing and NWP model delay estimation in one package, which simplifies the use of tropospheric corrections in InSAR time-series. Also, the radar geometry from InSAR processing can be used to compute NWP delay estimates, enabling the use of slant total delays (STD) rather than zenith total delays (ZTD). This can lead to a significant horizontal shift of delay patterns, although smaller than similar shifts due to timing errors of the NWP model (Yu et al., 2018; Mulder et al., 2025). Finally, the shared satellite geometry can also prevent problems due to the use of different or lower resolution DEMs in the tropospheric correction product (Zinno et al., 2023). However, these delay errors are limited to about 1 mm per 50 m DEM error (Cavalié et al., 2007; Jolivet et al., 2014) and are likely only significant in areas with strong elevation differences.

5.2. InSAR as input for NWP models

A less explored, but promising application the use of InSAR data to enhance weather forecasting. However, this is often difficult because InSAR data offers differential delays, while NWP models need absolute delay information. This problem can be solved by subtracting the NWP model delay for one date from the differential delays to derive the InSAR tropospheric delays at the other date (Mateus et al., 2018, 2020), but this method is very sensitive for errors in the NWP model. Therefore, more robust have been proposed (Liu, 2013; Mulder et al., 2022) based on time-series of InSAR and NWP model data, which can be provided by RIPPL. Additionally, results from the RIPPL software can be used to evaluate the performance and precision of NWP models at different weather states (Mulder et al., 2025, 2022). Finally, the integration of InSAR and NWP data can aid in analysing specific atmospheric conditions (Hanssen et al.). For example, these combined datasets can be used for statistical analysis of delay variations, offering insights into current weather states or potential atmospheric disturbances (Hanssen, 2001; Mulder et al., 2023).

6. Conclusion

As shown in the result section the RIPPL package offers a way to seamlessly integrate the processing of InSAR data stacks with the estimation of tropospheric delay based on NWP models. This allows for the use of the radar geometry needed for the InSAR processing to apply a ray-tracing method for the atmospheric delay estimation. Although our presented methods are mainly a combination of previously developed methods, we believe that the integration of InSAR and NWP model data processing not only improves the quality and comparability of the two products, but could also further the InSAR deformation and NWP model research. For InSAR research this can simplify the use of atmospheric corrections, because they are readily available in the same format. For NWP model research this can help to compare NWP model realizations with InSAR tropospheric delay measurements and a help develop methods to assimilate InSAR tropospheric measurements into NWP models.

CRediT authorship contribution statement

G. Mulder: Writing – review & editing, Writing – original draft, Visualization, Validation, Software, Methodology, Conceptualization. **F.J. van Leijen:** Writing – review & editing, Validation, Software. **P. Lopez-Dekker:** Writing – review & editing, Methodology. **R.F. Hanssen:** Writing – review & editing, Supervision, Funding acquisition.

Computer code availability

The RIPPL Python code is freely available from the TU Delft Geodesy GitHub repository via the following link. The RIPPL code is written in Python only, but it does depend on the installation of the Snaphu software to unwrap interferograms. Further required dependencies can be installed using one of the Python package managers. The tutorials and installation scripts are written as a jupyter notebook (Granger and Perez, 2021) and can therefore be run using the jupyter interface in a web browser. The total disk space of the RIPPL package is only 15 MB, but make sure that you have at least 100 GB of free disk space to run the tutorials, as the SAR SLCs and resampled SLCs take up a lot of disk space. To properly run the RIPPL code a minimum of 4 GB RAM is needed, but 16 GB is recommended. For any questions about the RIPPL code the corresponding author of this paper can be contacted.

Declaration of competing interest

The authors declare that they have no known competing financial interests or personal relationships that could have appeared to influence the work reported in this paper.

Acknowledgements

This project was enabled by the Dutch Research Council (NWO) under project ALW-GO/14-39.

Appendix A. Supplementary data

Supplementary material related to this article can be found online at https://doi.org/10.1016/j.cageo.2025.106069.

Data availability

The research code is freely available. The research data is freely available and can be downloaded from the data providers listed in Table 1 using the RIPPL software itself.

References

Bekaert, D.P.S., Walters, R.J., Wright, T.J., Hooper, A.J., Parker, D.J., 2015. Statistical comparison of InSAR tropospheric correction techniques. Remote Sens. Environ. 170, 40–47. http://dx.doi.org/10.1016/j.rse.2015.08.035.

Bengtsson, L., Andrae, U., Aspelien, T., Batrak, Y., Calvo, J., Rooy, W.d., Gleeson, E., Hansen-Sass, B., Homleid, M., Hortal, M., Ivarsson, K.I., Lenderink, G., Niemelä, S., Nielsen, K.P., Onvlee, J., Rontu, L., Samuelsson, P., Muñoz, D.S., Subias, A., Tijm, S., Toll, V., Yang, X., Koltzow, M.O., 2017. The HARMONIE-AROME model configuration in the ALADIN-HIRLAM NWP system. Mon. Weather Rev. 145 (5), 1919–1935. http://dx.doi.org/10.1175/MWR-D-16-0417.1.

Berardino, P., Fornaro, G., Lanari, R., Sansosti, E., 2002. A new algorithm for surface deformation monitoring based on small baseline differential SAR interferograms. IEEE Trans. Geosci. Remote Sens. 40 (11), 2375–2383. http://dx.doi.org/10.1109/TGRS.2002.803792, URL: http://ieeexplore.ieee.org/document/1166596/.

Bevis, M., Businger, S., Herring, T.a., Rocken, C., Anthes, R.a., Ware, R.H., 1992. GPS meteorology - Remote sensing of atmospheric water vapor using the Global Positioning System. J. Geophys. Res. 97 (92), 787–801. http://dx.doi.org/10.1029/92JD01517.

Cavalié, O., Doin, M.P., Lasserre, C., Briole, P., 2007. Ground motion measurement in the Lake Mead area, Nevada, by differential synthetic aperture radar interferometry time series analysis: Probing the lithosphere rheological structure. J. Geophys. Res.: Solid Earth 112 (3), http://dx.doi.org/10.1029/2006JB004344.

Chen, C., Zebker, H., 2002. Phase unwrapping for large SAR interferograms: statistical segmentation and generalized network models. IEEE Trans. Geosci. Remote Sens. 40 (8), 1709–1719. http://dx.doi.org/10.1109/TGRS.2002.802453, URL: http://ieeexplore.ieee.org/document/1036000/.

Dask Development Team, 2016. Dask: Library for dynamic task scheduling. URL: https://dask.org.

Davis, J.L., Herring, T.A., Shapiro, I.I., Rogers, A.E.E., Elgered, G., 1985. Geodesy by radio interferometry: Effects of atmospheric modeling errors on estimates of baseline length. Radio Sci. 20 (6), 1593–1607. http://dx.doi.org/10.1029/RS020i006p01593, URL: http://doi.wiley.com/10.1029/RS020i006p01593.

De Haan, S., 2008. Meteorological Applications of a Surface Network of Global Positioning System Receivers (Ph.D. thesis). Wageningen University, p. 143.

de Haan, S., Holleman, I., Holtslag, A.a.M., 2009. Real-time water vapor maps from a GPS surface network: Construction, validation, and applications. J. Appl. Meteorol. Clim. 48 (7), 1302–1316. http://dx.doi.org/10.1175/2008JAMC2024.1.

De Zan, F., Guarnieri, A.M., 2006. TOPSAR: Terrain observation by progressive scans. IEEE Trans. Geosci. Remote Sens. 44 (9), 2352–2360. http://dx.doi.org/10.1109/TGRS.2006.873853.

ECMWF, 2019. Copernicus climate data store. URL: https://cds.climate.copernicus.eu/cdsapp#!/home.

ESA, 2021a. Copernicus sentinel precise orbits data. URL: https://dataspace.copernicus.eu.

ESA, 2021b. SNAP - ESA sentinel application platform. URL: http://step.esa.int.

ESA, 2024. Copernicus sentinel data. URL: https://dataspace.copernicus.eu.

Farr, T.G., Rosen, P.A., Caro, E., Crippen, R., Duren, R., Hensley, S., Kobrick, M., Paller, M., Rodriguez, E., Roth, L., Seal, D., Shaffer, S., Shimada, J., Umland, J., Werner, M., Oskin, M., Burbank, D., Alsdorf, D., 2007. The shuttle radar topography mission. Rev. Geophys. 45 (2), RG2004. http://dx.doi.org/10.1029/2005RG000183, URL: http://doi.wiley.com/10.1029/2005RG000183.

Ferretti, A., Fumagalli, A., Novali, F., Prati, C., Rocca, F., Rucci, A., 2011. A new algorithm for processing interferometric data-stacks: SqueeSAR. IEEE Trans. Geosci. Remote Sens. 49 (9), 3460–3470. http://dx.doi.org/10.1109/TGRS.2011.2124465.

Ferretti, A., Prati, C., Rocca, F., 2001. Permanent scatterers in SAR interferometry. TGARS 39 (1), 8–20. http://dx.doi.org/10.1109/36.898661.

Geudtner, D., Schwäbisch, M., 1996. An algorithm for precise reconstruction of InSAR imaging geometry: Application to flat-earth phase removal, phase-to-height conversion and geocoding of InSAR-derived DEMs. In: Proc. EUSAR '96 (1996). URL: https://elib.dlr.de/23829/.

Goldstein, R.M., Werner, C.L., 1998. Radar interferogram filtering for geophysical applications. Geophys. Res. Lett. 25 (21), 4035–4038.

Granger, B.E., Perez, F., 2021. Jupyter: Thinking and storytelling with code and data. Comput. Sci. Eng. 23 (2), 7–14. http://dx.doi.org/10.1109/MCSE.2021.3059263.

Haji-Aghajany, S., Tasan, M., Izanlou, S., Rohm, W., 2025. TropoDeep: a deep learning-based model for InSAR tropospheric correction on large-scale interferograms using GNSS and WRF outputs. J. Geod. 99 (10), http://dx.doi.org/10.1007/s00190-025-02001-0.

Hanssen, R.F., 2001. Radar Interferometry: Data Interpretation and Error Analysis (Ph.D. thesis). Delft University of Technology, p. 308.

Hanssen, R.F., Weckwerth, T.M., Zebker, H.A., Klees, R., 1999. High-resolution water vapor mapping from interferometric radar measurements. Science 283, 1295–1297, URL: http://doris.tudelft.nl/Literature/hanssen99.pdf.

Harris, C.R., Millman, K.J., van der Walt, S.J., Gommers, R., Virtanen, P., Cournapeau, D., Wieser, E., Taylor, J., Berg, S., Smith, N.J., Kern, R., Picus, M., Hoyer, S., van Kerkwijk, M.H., Brett, M., Haldane, A., del Río, J., Wiebe, M., Peterson, P., Gérard-Marchant, P., Sheppard, K., Reddy, T., Weckesser, W., Abbasi, H., Gohlke, C., Oliphant, T.E., 2020. Array programming with {NumPy}. Nature 585, 357–362. http://dx.doi.org/10.1038/s41586-020-2649-2.

Hersbach, H., Bell, B., Berrisford, P., Hirahara, S., Horányi, A., Muñoz-Sabater, J., Nicolas, J., Peubey, C., Radu, R., Schepers, D., Simmons, A., Soci, C., Abdalla, S., Abellan, X., Balsamo, G., Bechtold, P., Biavati, G., Bidlot, J., Bonavita, M., De Chiara, G., Dahlgren, P., Dee, D., Diamantakis, M., Dragani, R., Flemming, J., Forbes, R., Fuentes, M., Geer, A., Haimberger, L., Healy, S., Hogan, R.J., Hólm, E., Janisková, M., Keeley, S., Laloyaux, P., Lopez, P., Lupu, C., Radnoti, G., de Rosnay, P., Rozum, I., Vamborg, F., Villaume, S., Thépaut, J.N., 2020. The ERA5 global reanalysis. Q. J. R. Meteorol. Soc. 146 (730), 1999–2049. http://dx.doi.org/10.1002/qj.3803.

Hooper, a., Segall, P., Zebker, H., 2007. Persistent scatterer interferometric synthetic aperture radar for crustal deformation analysis, with application to Volcán Alcedo, Galápagos. J. Geophys. Res.: Solid Earth 112 (7), 1–21. http://dx.doi.org/10.1029/2006JB004763.

Huuskonen, A., Holleman, I., 2007. Determining weather radar antenna pointing using signals detected from the sun at low antenna elevations. J. Atmos. Ocean. Technol. 24 (3), 476–483. http://dx.doi.org/10.1175/JTECH1978.1.

Jolivet, R., Agram, P.S., Lin, N.Y., Simons, M., Doin, M.-p., Peltzer, G., Li, Z., 2014. Improving InSAR geodesy using Global Atmospheric Models. J. Geophys. Res.: Solid Earth 119 (3), 2324–2341. http://dx.doi.org/10.1002/2013JB010588, URL: http://doi.wiley.com/10.1002/2013JB010588.

Jolivet, R., Grandin, R., Lasserre, C., Doin, M.-P., Peltzer, G., 2011. Systematic InSAR tropospheric phase delay corrections from global meteorological reanalysis data. Geophys. Res. Lett. 38 (17), n/a–n/a. http://dx.doi.org/10.1029/2011GL048757, URL: http://doi.wiley.com/10.1029/2011GL048757.

Kampes, B., Hanssen, R., 2004. Ambiguity resolution for permanent scatterer interferometry. IEEE Trans. Geosci. Remote Sens. 42 (11), 2446–2453. http://dx.doi.org/10.1109/TGRS.2004.835222, URL: http://ieeexplore.ieee.org/lpdocs/epic03/wrapper.htm?arnumber=1356058.

Kampes, B.M., Usai, S., 1999. Doris: The delft object-oriented radar interferometric software. URL: https://api.semanticscholar.org/CorpusID:13895987.

Liu, S., 2013. Satellite Radar Interferometry: Estimation of Atmospheric Delay (Ph.D. thesis). Delft University of Technology, p. 230.

Mateus, P., Catalao, J., Nico, G., Benevides, P., 2020. Mapping precipitable water vapor time series from Sentinel-1 interferometric SAR. IEEE Trans. Geosci. Remote Sens. 58 (2), 1373–1379. http://dx.doi.org/10.1109/TGRS.2019.2946077.

Mateus, P., Miranda, P.M.A., Nico, G., Catalão, J., Pinto, P., Tomé, R., 2018. Assimilating InSAR maps of water vapor to improve heavy rainfall forecasts: A case study with two successive storms. J. Geophys. Res.: Atmospheres 123 (7), 3341–3355. http://dx.doi.org/10.1002/2017JD027472, URL: http://doi.wiley.com/10.1002/2017JD027472.

Met Office, 2015. Cartopy: a cartographic python library with a Matplotlib interface. URL: https://scitools.org.uk/cartopy.

Meyer, F.J., 2011. Performance requirements for ionospheric correction of low-frequency SAR data. IEEE Trans. Geosci. Remote Sens. 49 (10), 3694–3702. http://dx.doi.org/10.1109/TGRS.2011.2146786, URL: http://ieeexplore.ieee.org/document/5783915/.

Moreira, A., Prats-Iraola, P., Younis, M., Krieger, G., Hajnsek, I., Papathanassiou, K.P., 2013. A tutorial on synthetic aperture radar. IEEE Geosci. Remote. Sens. Mag. 1 (1), 6–43. http://dx.doi.org/10.1109/MGRS.2013.2248301, URL: http://ieeexplore.ieee.org/lpdocs/epic03/wrapper.htm?arnumber=6504845.

Mulder, G., Barkmeijer, J., de Haan, S., van Leijen, F., Hanssen, R., 2025. On the use of InSAR for estimating timing errors in Harmonie-Arome water vapor fields. J. Geophys. Res.: Atmospheres 130 (1), http://dx.doi.org/10.1029/2023JD040566.

Mulder, G., Van Leijen, F.J., Barkmeijer, J., De Haan, S., Hanssen, R.F., 2022. Estimating single-epoch integrated atmospheric refractivity from InSAR for assimilation in numerical weather models. IEEE Trans. Geosci. Remote Sens. 1. http://dx.doi.org/10.1109/TGRS.2022.3177041, URL: https://ieeexplore.ieee.org/document/9779705/.

Mulder, G., Van Leijen, F.J., Hanssen, R.F., 2023. A generic approach to parameterize the turbulent energy of single-epoch atmospheric delays from InSAR time series. IEEE Trans. Geosci. Remote Sens. 61, http://dx.doi.org/10.1109/TGRS.2023.3295898.

Murray, K.D., Bekaert, D.P., Lohman, R.B., 2019. Tropospheric corrections for InSAR: Statistical assessments and applications to the Central United States and Mexico. Remote Sens. Environ. 232, http://dx.doi.org/10.1016/j.rse.2019.111326.

PROJ contributors, 2021. {PROJ} coordinate transformation software library. URL: https://proj.org/.

Ridal, M., Bazile, E., Le Moigne, P., Randriamampianina, R., Schimanke, S., Andrae, U., Berggren, L., Brousseau, P., Dahlgren, P., Edvinsson, L., El-Said, A., Glinton, M., Hagelin, S., Hopsch, S., Isaksson, L., Medeiros, P., Olsson, E., Unden, P., Wang, Z.Q., 2024. CERRA, the copernicus European regional reanalysis system. Q. J. R. Meteorol. Soc. http://dx.doi.org/10.1002/qj.4764.

Rizzoli, P., Martone, M., Gonzalez, C., Wecklich, C., Borla Tridon, D., Bräutigam, B., Bachmann, M., Schulze, D., Fritz, T., Huber, M., Wessel, B., Krieger, G., Zink, M., Moreira, A., 2017. Generation and performance assessment of the global TanDEM-X digital elevation model. ISPRS J. Photogramm. Remote Sens. 132, 119–139. http://dx.doi.org/10.1016/j.isprsjprs.2017.08.008.

Rosen, P.A., Gurrola, E.M., Agram, P.S., Sacco, G.F., Lavalle, M., 2015. The InSAR Scientific Computing Environment (ISCE): A Python framework for earth science. In: AGU Fall Meeting Abstracts. pp. IN11C–1789.

Sandwell, D., Mellors, R., Tong, X., Wei, M., Wessel, P., 2011. Open radar interferometry software for mapping surface Deformation. Eos Trans. Am. Geophys. Union 92 (28), 234. http://dx.doi.org/10.1029/2011EO280002, URL: https://onlinelibrary.wiley.com/doi/abs/10.1029/2011EO280002.

Sansosti, E., Berardino, P., Manunta, M., Serafino, F., Fornaro, G., 2006. Geometrical SAR image registration. IEEE Trans. Geosci. Remote Sens. 44 (10), 2861–2870. http://dx.doi.org/10.1109/TGRS.2006.875787, URL: http://ieeexplore.ieee.org/document/1704979/.

Thayer, G.D., 1967. A rapid and accurate ray tracing algorithm for a horizontally stratified atmosphere. Radio Sci. 2 (2), 249–252. http://dx.doi.org/10.1002/rds196722249, URL: https://agupubs.onlinelibrary.wiley.com/doi/10.1002/rds196722249.

Touzi, R., Lopes, A., Bruniquel, J., Vachon, P., 1999. Coherence estimation for SAR imagery. IEEE Trans. Geosci. Remote Sens. 37 (1), 135–149. http://dx.doi.org/10.1109/36.739146, URL: http://ieeexplore.ieee.org/document/739146/.

Virtanen, P., Gommers, R., Oliphant, T.E., Haberland, M., Reddy, T., Cournapeau, D., Burovski, E., Peterson, P., Weckesser, W., Bright, J., van der Walt, S.J., Brett, M., Wilson, J., Millman, K.J., Mayorov, N., Nelson, A.R.J., Jones, E., Kern, R., Larson, E., Carey, C.J., Polat, İ., Feng, Y., Moore, E.W., VanderPlas, J., Laxalde, D., Perktold, J., Cimrman, R., Henriksen, I., Quintero, E.A., Harris, C.R., Archibald, A.M., Ribeiro, A.H., Pedregosa, F., van Mulbregt, P., SciPy 1.0 Contributors, 2020. {SciPy} 1.0: Fundamental algorithms for scientific computing in Python. Nature Methods 17, 261–272. http://dx.doi.org/10.1038/s41592-019-0686-2.

Wegmüller, U., Werner, C., 1997. Gamma SAR processor and interferometry software. In: European Space Agency, (Special Publication) ESA SP. pp. 1687–1692, URL: https://www.scopus.com/inward/record.uri?eid=2-s2.0-52442237398&partnerID=40&md5=1687c77ce58f9c3391546be124f531a4.

Yague-Martinez, N., Prats-Iraola, P., Rodriguez Gonzalez, F., Brcic, R., Shau, R., Geudtner, D., Eineder, M., Bamler, R., 2016. Interferometric processing of Sentinel-1 TOPS data. IEEE Trans. Geosci. Remote Sens. 54 (4), 2220–2234. http://dx.doi.org/10.1109/TGRS.2015.2497902, URL: http://proceedings.esa.int/fringe2015/page_paper116.php http://ieeexplore.ieee.org/document/7390052/.

Yu, C., Li, Z., Penna, N.T., Crippa, P., 2018. Generic atmospheric correction model for interferometric synthetic aperture radar observations. J. Geophys. Res.: Solid Earth 123 (10), 9202–9222. http://dx.doi.org/10.1029/2017JB015305, URL: https://onlinelibrary.wiley.com/doi/10.1029/2017JB015305.

Zhou, H., Dai, K., Pirasteh, S., Li, R., Xiang, J., Li, Z., 2023. InSAR spatial-heterogeneity tropospheric delay correction in steep mountainous areas based on deep learning for landslides monitoring. IEEE Trans. Geosci. Remote Sens. 61, http://dx.doi.org/10.1109/TGRS.2023.3307477.

Zinno, I., Casamento, F., Lanari, R., 2023. On the exploitation of etad data for the atmospheric phase screen filtering of medium/high resolution dinsar products. In: International Geoscience and Remote Sensing Symposium. IGARSS, Institute of Electrical and Electronics Engineers Inc., pp. 7882–7885. http://dx.doi.org/10.1109/IGARSS52108.2023.10281591.